The Astrophysical Journal, 844:49 (14pp), 2017 July 20 https://doi.org/10.3847/1538-4357/aa7875
© 2017. The American Astronomical Society. All rights reserved.

GASP. II. A MUSE View of Extreme Ram-Pressure Stripping along the Line of Sight: Kinematics of the Jellyfish Galaxy JO201

C. Bellhouse[1,2], Y. L. Jaffé [2], G. K. T. Hau [2], S. L. McGee[1], B. M. Poggianti[3], A. Moretti[3], M. Gullieuszik[3], D. Bettoni[3], G. Fasano[3], M. D'Onofrio[3,4], J. Fritz[5], A. Omizzolo[3,6], Y.-K. Sheen[7], and B. Vulcani[8,3]
[1] University of Birmingham School of Physics and Astronomy, Edgbaston, Birmingham, UK; cbellhou@eso.org
[2] European Southern Observatory, Alonso de Cordova 3107, Vitacura, Casilla 19001, Santiago de Chile, Chile
[3] INAF—Astronomical Observatory of Padova, Vicolo dell'Osservatorio 5, I-35122 Padova, Italy
[4] Dipartimento di Fisica & Astronomia Galileo Galilei, Università di Padova, Vicolo dell'Osservatorio 3, I-35122 Padova, Italy
[5] Instituto de Radioastronomía y Astrofísica, Morelia, Mexico
[6] Specola Vaticana, 00120, Vatican City, Vatican City State
[7] Korea Astronomy and Space Science Institute, 766, Daedeokdae-ro, Yuseong-gu, Daejeon, 34055, Korea
[8] School of Physics, University of Melbourne, Melbourne, VIC 3010, Australia
Received 2017 January 16; revised 2017 April 6; accepted 2017 April 17; published 2017 July 20

Abstract

This paper presents a spatially resolved kinematic study of the jellyfish galaxy JO201, one of the most spectacular cases of ram-pressure stripping (RPS) in the GAs Stripping Phenomena in galaxies with MUSE (GASP) survey. By studying the environment of JO201, we find that it is moving through the dense intracluster medium of Abell 85 at supersonic speeds along our line of sight, and that it is likely accompanied by a small group of galaxies. Given the density of the intracluster medium and the galaxy's mass, projected position, and velocity within the cluster, we estimate that JO201 must so far have lost ∼50% of its gas during infall via RPS. The MUSE data indeed reveal a smooth stellar disk accompanied by large projected tails of ionized (Hα) gas, composed of kinematically cold (velocity dispersion $<40\,\mathrm{km\,s^{-1}}$) star-forming knots and very warm ($>100\,\mathrm{km\,s^{-1}}$) diffuse emission, that extend out to at least ∼50 kpc from the galaxy center. The ionized Hα-emitting gas in the disk rotates with the stars out to ∼6 kpc; but, in the disk outskirts, it becomes increasingly redshifted with respect to the (undisturbed) stellar disk. The observed disturbances are consistent with the presence of gas trailing behind the stellar component resulting from intense face-on RPS along the line of sight. Our kinematic analysis is consistent with the estimated fraction of lost gas and reveals that stripping of the disk happens outside-in, causing shock heating and gas compression in the stripped tails.

Key words: galaxies: clusters: general – galaxies: evolution – galaxies: ISM – galaxies: kinematics and dynamics – techniques: imaging spectroscopy

Supporting material: interactive figure

1. Introduction

The evolution of galaxies is driven by a combination of internal and environmental processes. Important discoveries from past decades supporting this idea include the observation that galaxy morphology and color correlate with both environmental density and galaxy mass (e.g., Dressler 1980; Baldry et al. 2006; Peng et al. 2010). Internal processes affecting the evolution of galaxies include stellar feedback from high-wind stars such as Wolf–Rayet and OB-type stars, supernova feedback, and the effects of active galactic nucleus (AGN) activity (Veilleux et al. 2005; Ho et al. 2014). Environmental processes can be separated into two categories: gravitational and hydrodynamical. Among the gravitational effects are tidal interactions between galaxies, common in moderately crowded environments (Spitzer & Baade 1951; Toomre 1977; Tinsley & Larson 1979; Merritt 1983; Mihos & Hernquist 1994; Springel 2000). In higher-mass clusters, the galaxies may also be subjected to perturbation by the gravitational potential of the cluster as a whole (Byrd & Valtonen 1990; Valluri 1993), giving rise to inflows as well as boosting star formation within the nuclear and disk regions. Over extended periods of time, cluster galaxies can also be affected by cumulative high-speed close-approach encounters with other cluster members (harassment; Moore et al. 1996, 1998). Hydrodynamical interactions between galaxies and the intracluster medium (ICM) can remove their halo gas via starvation/strangulation (Larson et al. 1980; Balogh et al. 2000) or their interstellar gas via ram-pressure stripping (RPS; Gunn & Gott 1972; Takeda et al. 1984; Faltenbacher & Diemand 2006). Additional mechanisms, such as thermal evaporation, have also been proposed (Cowie & Songaila 1977). We refer to Boselli & Gavazzi (2006) for a review of all of the environmental effects. In this paper, we focus on the effect of RPS on the gas loss of cluster galaxies.

In a seminal paper, Gunn & Gott (1972) showed that the ram pressure exerted by the ICM on an infalling galaxy is proportional to the medium density and the square of the velocity of the galaxy relative to it ($P_{\mathrm{ram}} \propto \rho v^2$). The galaxy will lose its gas if ram pressure overcomes the limiting force per unit area, which depends on the surface density. This description, although simplified, reproduces the observed gas deficiencies of cluster galaxies very well (see, e.g., Chung et al. 2007; Jaffé et al. 2015). Recent hydrodynamical simulations have shown, however, that the efficiency of RPS is a function of the inclination, with face-on encounters being typically more efficient at stripping than edge-on or inclined encounters (Abadi et al. 1999; Quilis et al. 2000; Vollmer et al. 2001). Some studies further suggest that gas removal by RPS may be accompanied by an enhancement in the star formation activity in the galaxy, as thermal instabilities and turbulent motions

within the galaxy provoke collapse within cold clouds (Evrard 1991; Bekki & Couch 2003). In fact, during the stripping phase, galaxies can exhibit largely disturbed optical or ultraviolet tails composed of young stars formed in situ in the stripped gas (Kenney & Koopmann 1999; Cortese et al. 2007; Yoshida et al. 2008; Hester et al. 2010; Smith et al. 2010; Yagi et al. 2010; Owers et al. 2012; Ebeling et al. 2014; Fumagalli et al. 2014; Kenney et al. 2014; Rawle et al. 2014; McPartland et al. 2016), for which they are often referred to as "jellyfish" galaxies. After the active stripping period has passed and a significant portion of the galaxy's gas has been lost to the ICM, the quenching of its star formation becomes inevitable (Fujita 1998; Fujita & Nagashima 1999; Vollmer et al. 2012; Haines et al. 2015; Jaffé et al. 2016).

The most convincing examples of RPS at play come from observations of neutral atomic hydrogen gas (H I) in cluster galaxies that display "tails" of gas trailing from the stellar continuum and reduced gas fractions that have convincingly demonstrated the efficiency of RPS (e.g., Haynes & Giovanelli 1984; Cayatte et al. 1990; Verdes-Montenegro et al. 2001; Kenney et al. 2004; Chung et al. 2009; Cortese et al. 2010; Yoon et al. 2017). Molecular gas studies show that, while this component is vulnerable to RPS, it is much less affected than atomic gas (Kenney & Young 1989; Boselli et al. 1997, 2014). An increasing number of studies of the ionized gas in jellyfish galaxies are also contributing to the understanding of the impact of RPS on star formation (Gavazzi et al. 2002; Yagi et al. 2010; Fossati et al. 2012; Boselli et al. 2016), with integral-field observations being particularly insightful (Merluzzi et al. 2013; Fumagalli et al. 2014; Fossati et al. 2016). Finally, jellyfish galaxies have been successfully reproduced by hydrodynamical simulations of RPS (Roediger & Brüggen 2007; Tonnesen & Bryan 2009, 2010, 2012).

We present results from a new Multi Unit Spectroscopic Explorer (MUSE; Bacon et al. 2010) survey at the Very Large Telescope (VLT) called GAs Stripping Phenomena in galaxies with MUSE (GASP[9]) that aims to provide a detailed systematic study of gas removal processes in galaxies (see Poggianti et al. 2017; Paper I). GASP is observing over 100 galaxies from the sample of jellyfish candidates of Poggianti et al. (2016), who visually selected galaxies with signatures of stripping from optical images of the WIde-field Nearby Galaxy-cluster Survey (WINGS; Fasano et al. 2006; Moretti et al. 2014), its extension OmegaWINGS (Gullieuszik et al. 2015; Moretti et al. 2017), and the Padova-Millennium Galaxy and Group Catalog (Calvi et al. 2011). The sample thus spans a wide range of stellar masses ($10^{9.2}$–$10^{11.5}\,M_{\odot}$) and environments (host dark matter halos of 10^{11}–$10^{15}\,M_{\odot}$).

In this paper, we present a kinematical analysis of one of the most spectacular jellyfish galaxies in GASP, JO201 (WINGS J004130.30–091546.1, also known as PGC 2456 and KAZ 364; R.A. 00:41:30.325, decl. − 09:15:45.96), a heavily ram-pressure-stripped galaxy in the massive galaxy cluster Abell 85. In Section 2, we summarize the properties of JO201 and present a study of its local and global environment. In Section 3, we describe the GASP MUSE observations, the data reduction process, and the corrections used for Galactic extinction. Section 4 focuses on the Hα emission-line fitting processes and shows the resulting Hα emission maps. Section 5 presents the stellar and ionized gas kinematics of the galaxy, including velocity and velocity dispersion maps, as well as rotation curves. Finally, in Section 6, we summarize all of the results and draw conclusions.

Unless otherwise stated, throughout the paper, we adopt a Chabrier initial mass function (IMF; Chabrier 2003) and a concordance ΛCDM cosmology of $\Omega_{\rm M} = 0.3$, $\Omega_{\Lambda} = 0.7$, $\rm H_0 = 70\ km\ s^{-1}\ Mpc^{-1}$.

2. JO201 and Its Environment

JO201 is perhaps the most convincing case of gas stripping in the sample of 419 (344 cluster and 75 field) jellyfish candidates of Poggianti et al. (2016). Its morphology is that of a spiral galaxy with tails of material to one side, and its total stellar mass is $3.55^{+1.24}_{-0.32} \times 10^{10}\,M_{\odot}$.

X-ray studies have classified JO201 as a Seyfert galaxy (Durret et al. 2005). Our MUSE observations confirm the presence of an AGN (see, e.g., broadened emission lines at the center of the galaxy in Section 4), but we leave the study of the AGN activity in JO201 for another paper (C. Bellhouse et al. 2017, in preparation).

JO201 resides in Abell 85, a massive cluster with a velocity dispersion of $\sigma_{cl} = 982 \pm 55\ \rm km\ s^{-1}$ ($M_{200} = 1.58 \times 10^{15}\,M_{\odot}$) at a redshift of $z_{\rm cl} = 0.05586$ (Moretti et al. 2017). This cluster is part of OmegaWINGS and therefore has wide-field OmegaCam imaging ($\sim$1 deg^2) and spectroscopy from the Anglo-Australian Telescope. JO201 is located very close to the brightest cluster galaxy (BCG) with a projected radial distance (r_{cl}) of only 360 kpc ($0.15 \times R_{200}$), as can be seen in Figure 1. Moreover, JO201 has a very high line-of-sight velocity with respect to the mean velocity of the cluster ($|\Delta v_{cl}| = 3363.7\ \rm km\ s^{-1} = 3.4 \times \sigma_{cl}$). In fact, it is outside the velocity cut originally considered for cluster membership ($3 \times \sigma_{cl}$; Moretti et al. 2017; Cava et al. 2009).

The left panel of Figure 2 shows the projected position-versus-velocity phase-space diagram of galaxies in Abell 85. All of the cluster members with a spectroscopic redshift in Abell 85 are overplotted (gray circles) on the distribution of all of the OmegaWINGS clusters stacked together (hex plot) and lie mostly within the trumpet-shaped region defined by the escape velocity of a Navarro et al. (1996) halo profile (gray curves). In this diagram, JO201 (magenta star) lies very close to the central region of the cluster in the "envelope" of the trumpet, which suggests that this galaxy is likely falling into the cluster for the first time. Its high peculiar velocity combined with its small r_{cl} also indicates a highly radial orbit. It is worth noting that JO201 is the most-central and fastest-traveling cluster jellyfish galaxy from the sample of Poggianti et al. (2016; see Y. L. Jaffé et al. 2017, in preparation).

Its location in phase space suggests that the galaxy is falling into the cluster from behind and moving toward the observer. Although the line-of-sight component probably dominates the velocity vector, the galaxy's projected tails point eastward (close to the direction of the BCG; see Figure 1), further suggesting that the velocity vector must have some inclination with respect to the line of sight.

We quantify the ram-pressure intensity exerted on JO201 by the ICM in the same manner as Jaffé et al. (2015). We utilize the cluster gas density distribution of Abell 85 presented in Bravo-Alfaro et al. (2009), computed from a hydrostatic-isothermal β-model (Cavaliere & Fusco-Femiano 1976) as

$$\rho(r) = \rho_0[1 + (r_{cl}/r_c)^2]^{-3\beta/2}, \quad (1)$$

[9] web.oapd.inaf.it/gasp

where the core radius $r_c = 82$ kpc, the central density $\rho_0 = 0.0257\,\mathrm{cm}^{-3}$, and $\beta = 0.532$ (values from Chen et al. 2007). The ram pressure exerted on JO201 can be computed following Gunn & Gott (1972)'s equation $P_{\rm ram} = \rho_{\rm ICM} \times v^2$, where $\rho_{\rm ICM}$ is the density of the ICM at the galaxy's position in the cluster and v is the galaxy's velocity relative to the ICM. We adopt the projected clustercentric distance (r_{cl}) and the line-of-sight differential velocity of the galaxy ($|\Delta v_{cl}|$) and obtain $P_{\rm ram}(\mathrm{JO201}) = 1.24 \times 10^{-11}\,\mathrm{Nm}^{-2}$. Note that, due to the mass of Abell 85 and the extreme speed of JO201, this value is over an order of magnitude higher than the estimated pressures computed for Virgo galaxies with H I tails in Chung et al. (2007).

We can then compare the ram pressure exerted by the ICM on the infalling galaxy with the anchoring self-gravity provided by the galaxy, defined as

$$\Pi_{\rm gal} = 2\pi G \Sigma_{\rm s} \Sigma_{\rm g}, \tag{2}$$

where $\Sigma_{\rm s}$ and $\Sigma_{\rm g}$ are the density profiles of the stellar and gaseous exponential disks, respectively, that can be expressed as

$$\Sigma = \left(\frac{M_d}{2\pi r_d^2}\right) e^{-r/r_d}, \tag{3}$$

where M_d is the disk mass, r_d is the disk scale length, and r is the radial distance from the center of the galaxy. For the stellar component of JO201, we adopt a disk mass $M_{d,\rm stars} = 3.55 \times 10^{10} M_\odot$ and a disk scale length $r_{d,\rm stars} = 5.56$ kpc, obtained by fitting the light profile of the galaxy from the V-band WINGS image.[10] For the gas component, we assume a total mass $M_{d,\rm gas} = 0.1 \times M_{d,\rm stars}$ and scale length $r_{d,\rm gas} = 1.7 \times r_{d,\rm stars}$ (Boselli & Gavazzi 2006).

These values yield $P_{\rm ram} = 0.008 \times \Pi_{\rm gal}$ at the center of the galaxy, which is not enough to strip the inner gas. The condition for stripping ($P_{\rm ram}/\Pi_{\rm gal} > 1$) is met only when considering that the galaxy is partially stripped (outside-in) down to a given "truncation radius," r_t.

By combining the stripping condition with Equations (2) and (3) at $r = r_t > 0$, we find that, at the location of JO201 in phase space, $P_{\rm ram}$ should have stripped the gas in JO201 down to $r_t \simeq 9$ kpc, which is equivalent to ∼50% of the total gas mass stripped, estimated from the equation for the remaining gas mass:

$$f = 1 + \left[e^{-r_t/r_d}\left(\frac{-r_t}{r_d} - 1\right)\right]. \tag{4}$$

This is shown in the phase-space diagram of Figure 2 (left), where JO201 (magenta star) sits on top of the line corresponding to 50% gas stripping of JO201 in Abell 85 (solid blue lines). We also plot the region corresponding to 20% of gas stripping (dashed blue lines; $r_t \simeq 17$ kpc) as a reference for the trajectory and stripping history of JO201 in phase space. As we will see in Section 5.3, the extent of the nonstripped Hα-emitting disk

[10] We note that, although the light-profile fitting reveals that JO201 is dominated by a disk component, there is a non-negligible bulge component (20% of the light) that we ignore when estimating the RPS intensity across the galaxy. The bulge component, however, is confined to the central part of the galaxy. We also note that the value of R_d obtained from V-band photometry is consistent with fits made to the stellar continuum (near Hα) using the MUSE data cube.

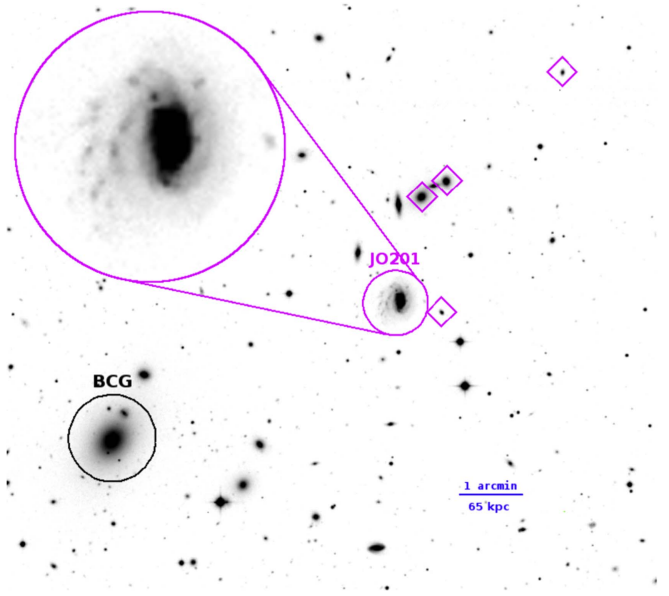

Figure 1. WINGS V-band image showing the central part of Abell 85. Highlighted are the BCG (black circle) and the jellyfish galaxy JO201 (magenta circle and inset) and its possible group companions (magenta diamonds), selected from their kinematical deviations as described in the text. The distance between JO201 and the BCG is ∼5.′6 (360 kpc at the redshift of the cluster). East is to the left and north to the top.

($r \gtrsim 6$ kpc along the major axis) is comparable to the estimated r_t. Note, however, that r_t is particularly difficult to measure in this galaxy due to the direction of stripping (see Sections 4 and 5).

We further study the local environment of JO201 by investigating the presence of substructures within Abell 85. We perform a Dressler–Shectman test (Dressler & Shectman 1988) that consists of computing individual galaxy deviations by comparing the local (nearest neighbors) velocity and velocity dispersion for each galaxy with the global (cluster) values. We characterize the cluster by its mean velocity ($\bar{v}_{\rm cl}$), velocity dispersion ($\sigma_{\rm cl}$), and total number of cluster members ($N_{\rm mem}$). Then, for each galaxy with $|\Delta v_{cl}| < 4 \times \sigma_{cl}$ (this cut includes galaxies with borderline membership, like JO201), we select a subsample of galaxies containing the galaxy i, plus its nearest 10 neighbors, and compute their mean velocity $\bar{v}^i_{\rm local}$ and velocity dispersion $\sigma^i_{\rm local}$. From these, we compute the individual galaxy deviations δ_i, following

$$\delta_i^2 = \left(\frac{10+1}{\sigma_{\rm cl}^2}\right)[(\bar{v}^i_{\rm local} - \bar{v}_{\rm cl})^2 + (\sigma^i_{\rm local} - \sigma_{\rm cl})^2]. \tag{5}$$

One way to investigate whether the cluster is substructured is through the "critical value" method, which compares $\Delta = \sum(\delta_i)$ with $N_{\rm mem}$. For Abell 85, $\Delta/N_{\rm mem} = 1.7$, and, as explained in Dressler & Shectman (1988), a value >1 is found in clusters with significant amounts of substructure.

The computed individual δ_i values are shown in the right panel of Figure 2, where groups of galaxies with high-velocity deviations ($\delta_i > 2.5$, as indicated by the dashed line in the histogram) are considered potential groups. According to this criterion, several substructures are visible (e.g., at the center and southeast). Our results are consistent with previous optical studies of Abell 85, such as Bravo-Alfaro et al. (2009). Moreover, the high level of substructure found in Abell 85 is in agreement with the findings of

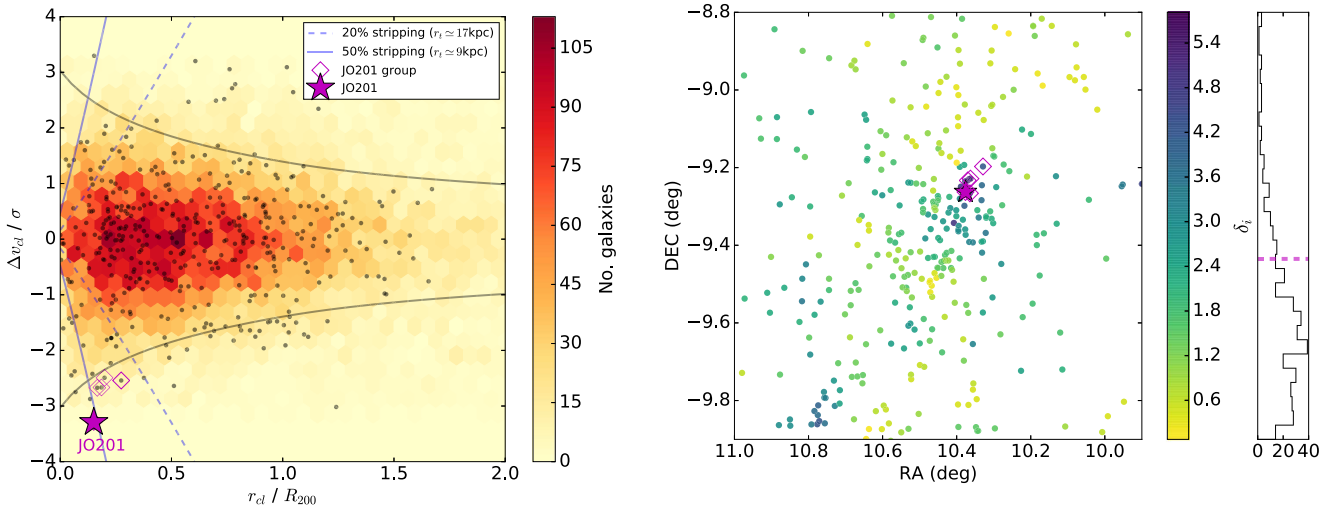

Figure 2. Left: projected phase-space diagram of all of the OmegaWINGS clusters (background density plot), where galaxies in Abell 85 are highlighted with gray circles. The gray curves represent the escape velocity in a Navarro et al. (1996) halo profile. The dashed and solid blue curves represent RPS models of JO201 by Abell 85's ICM in which 20% or 50% of the total gas mass in the disk has been removed (see the text for details). Right: Dressler–Shectman "bubble" plot showing the spatial distribution of galaxies in Abell 85, color-coded by their velocity deviations δ_i. The magenta dashed line on the histogram shows $\delta_i = 2.5$, above which a galaxy may be considered part of a group or substructure. In both panels, JO201 is marked with a magenta star, and its possible group companions are indicated with magenta diamonds.

Ichinohe et al. (2015), who studied the cluster's X-ray emission and concluded that the cluster has undergone a merger event in the past, in addition to at least two currently ongoing mergers with galaxy groups.

To test whether JO201 is part of a substructure, we select galaxies in its vicinity with $\delta_i > 2.5$ and study their velocity distribution. We find that four of these galaxies are likely forming a group with JO201, since they have similar line-of-sight velocities (see left panel of Figure 2). These galaxies are highlighted in Figures 1 and 2 with magenta diamonds.

In summary, JO201 is a massive spiral falling into the massive galaxy cluster Abell 85 within a small group of galaxies. Its projected position and velocity within the cluster suggest that it is crossing the cluster at supersonic speed in a radial orbit. The galaxy's motion through the cluster invokes ram pressure on its disk, which has caused significant gas stripping (∼50% of the total gas mass). In the following sections, we study the effects of RPS on this galaxy by comparing the distribution and kinematics of ionized Hα gas with that of stars.

3. Data

3.1. MUSE Observations

JO201 was observed on 2015 December 17 with photometric conditions and image quality of ∼0.″7 FWHM, as measured from the stars in the slow-guiding system surrounding the MUSE field of view (see MUSE user manual[11]). A total of eight 675 s exposures spanning two adjacent fields were observed with the nominal mode with an instrument rotation of 90° and a small spatial offset between exposures, as recommended by the MUSE user manual. An internal illumination flat field was taken at the beginning of the observations for the purpose of illumination correction. A spectrophotometric standard star, GD-71, was also observed right after the science target for flux calibration and telluric correction. Standard calibration files per the MUSE calibration plan were also taken.

3.2. Data Reduction

For the data reduction, we followed the standard reduction procedures as described in the pipeline manual (Bacon et al. 2010; http://www.eso.org/sci/software/pipelines/muse), with minor exceptions. We used custom scripts for organizing and preparing the raw data, which were then fed to ESOREX recipes version 3.12, MUSE pipeline version 1.2.1. As the data had sufficient sky coverage, the sky was modeled directly and subtracted from individual frames using the 20% pixels with the lowest counts. After wavelength calibration using arc lamp exposures, the final wavelength adjustments were made using sky emission lines. The final flux-calibrated data cube was generated by lining up and combining the individual frames using sources in the white light images. The final image quality is 0.″8 FWHM in the reduced cube.

The full GASP data reduction process is described in greater detail in Paper I.

An RGB image produced using the reduced MUSE cube is shown in Figure 3. Visible in the image are a series of bright knots to the east of the galaxy connected by "bridges" of diffuse emission, as well as slight morphological asymmetry in the disk. The western side of the disk shows a bright ridge of emission along an arc-shaped pattern, suggestive of a bowshock increasing the star formation activity in the leading edge. On the far left of the image are bright knots that are far from the disk of the galaxy and are likely to have been stripped at a much earlier stage.

3.3. Galactic Extinction Correction

The observed spectra are subject to reddening by dust in the Milky Way, which must be accounted for prior to any analysis of the emission-line fluxes. For the correction to be made, the amount of dust visible in the observed line of sight must be quantified. We estimated the contribution of dust using values from the galactic dust extinction and reddening tool in the

[11] http://www.eso.org/sci/facilities/paranal/instruments/muse/doc.html

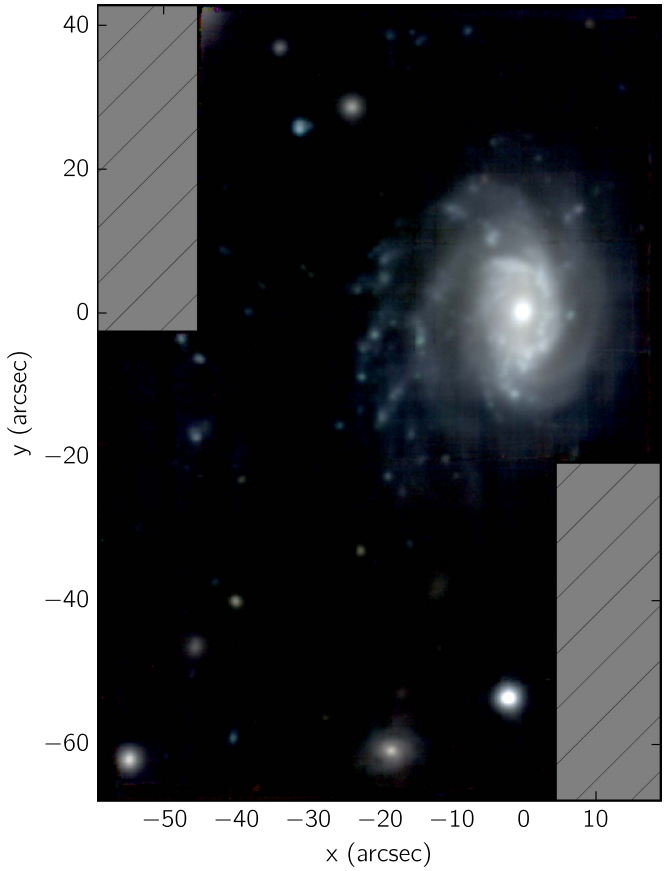

Figure 3. RGB image from JO201 GASP observation produced using 1000 Å slices integrated from the data cube (B: 5000–6000 Å, G: 6000–7000 Å, R: 7000–8000 Å). East is to the left and north to the top. A series of bright knots to the east of the galaxy are connected by "bridges" of diffuse emission. The asymmetry of the disk and brightening of the western edge are suggestive of a bowshock increasing the star formation activity in the leading edge. On the far left are bright knots that are far removed from the galaxy and likely to have been stripped at a much earlier stage.

NASA/IRSA infrared science archive, which uses measurements from Schlafly & Finkbeiner (2011) to quantify the dust distribution and give an extinction estimate across the cube. The obtained extinction of $E(B-V) = 0.0319$, $A_V = 0.0987$ was used in the Cardelli extinction law (Cardelli et al. 1989) to obtain a correction that was applied to the spectrum of each spaxel across the cube. The corrected cube was then used in all subsequent analyses.

4. Emission-line Fitting

By fitting model profiles to the emission lines, the spatial distribution of different emission lines, as well as the peculiar velocity and velocity dispersion of the emitting gas, can be derived. In order to fit emission lines, the IDL custom code KUBEVIZ (Fossati et al. 2016), written by Matteo Fossati and David Wilman, was used. The KUBEVIZ code fits a set of predefined emission lines across the spectrum using models with up to two Gaussian components or using moments.

4.1. Single-component Fits

The available lines in the fitting procedure were Hβ, [O III], [O I], [N II], Hα, and [S II]; however, this paper will focus on the Hα (λ6563) emission, fitted alongside the [N II] (λ6548, 6583) lines. A later paper will cover the full range of emission lines. The line fitting was carried out on a cube smoothed spatially using the mean value within a 3 × 3 kernel.

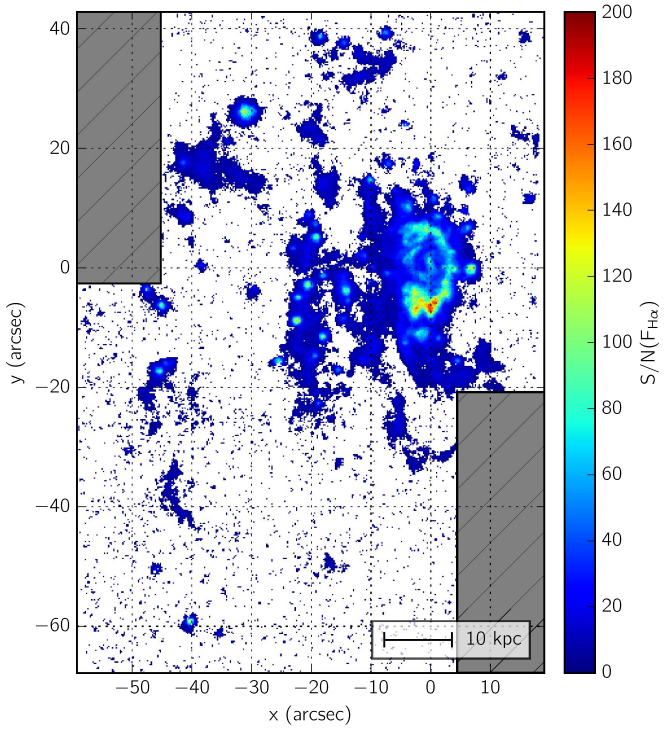

Figure 4. Hα S/N map calculated from the line fits to the MUSE data. The higher S/Ns are seen in the areas of brightest Hα emission in the western edge of the galactic disk and in the knots located east of the disk. All fitted spaxels are shown, with no signal noise cutoff applied.

The redshift used for fitting the lines in KUBEVIZ was set at $z = 0.045$, calculated by KUBEVIZ using the spectral position of the Hα line at the central point of the galactic disk.

As the noise values in the "stat" data cube produced by the MUSE pipeline underestimate the total error, the option was selected in KUBEVIZ to compute the nominal standard deviations of the measurements after renormalizing the covariance matrix, assuming a reduced $\chi^2 = 1$ (Fossati et al. 2016). The continuum under each line was calculated between 80 and 200 Å from each line, omitting regions containing other known emission lines and using values within the 40th and 60th percentiles. An initial value of 20 km s^{-1} was set for the narrow line width to prevent KUBEVIZ from returning an error when fitting regions with low velocity dispersion, in particular the upper region of the galactic disk and the central region of the star-forming knot to the northeast of the field.

Figure 4 shows the Hα signal-to-noise ratio (S/N) map resulting from the line fits. We rejected fits with S/N < 3, as well as unrealistic fits flagged by KUBEVIZ, which have zero velocity or velocity error.

For each fitted spaxel, the fitting process yielded a central wavelength, intensity, and width of the Hα line that could in turn be converted into velocity, flux, and velocity dispersion.

We visually inspected the emission-line fits and found that, in most cases, they describe the line profiles well. In some regions, however, the line profiles are more complex, and thus multicomponent fits are needed. Three example spectra extracted from different spaxels within the galaxy are shown in Figure 5. The top panel shows the central region of the galaxy,

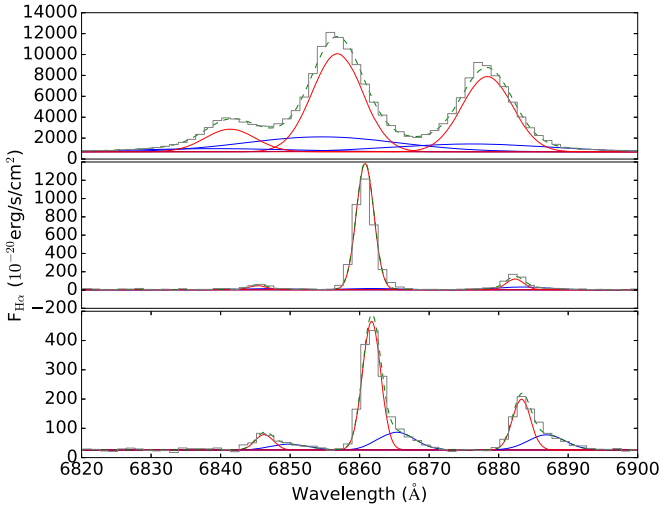

Figure 5. Observed Hα, N II emission-line group in three different spaxels within JO201 (black histograms), together with a two-component fit (the red and blue curves correspond to individual components, and the green dashed line is their sum). Top panel: central region of the galaxy, broadened by the AGN. Middle panel: region within the northeastern star-forming blob. Bottom panel: region in the outer part of the disk displaying obvious tails redward of the emission.

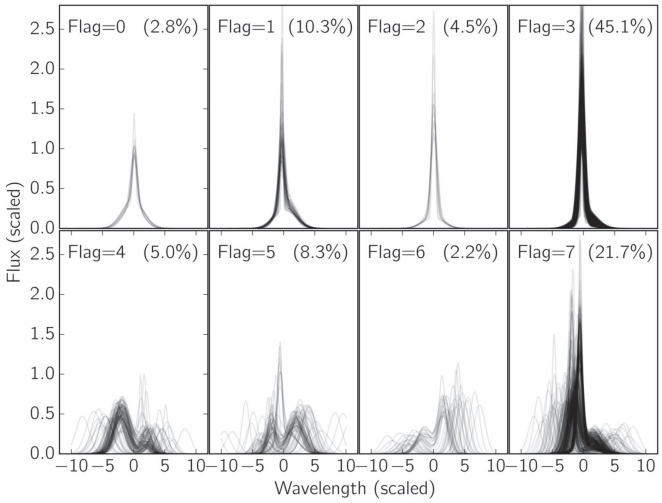

Figure 6. Profiles of double-component fits made to Hα emission lines in JO201, separated into the combined flags described in Section 4.2. Each of the plotted profiles has been normalized in position width and height to facilitate the comparison of the shape of the profiles. Percentages show the number of spaxels with each flag value out of the total number of spaxels fitted with two components. The flag values are mapped in the context of the galaxy in Figure 7.

where an AGN has clearly broadened the lines. In this case, two Gaussian components (red and blue lines) fit the emission lines better than a single component. The middle panel shows a star-forming region (large Hα blob with high S/N northeast of the galaxy disk, visible in Figure 4) well fitted by a single Gaussian. In the bottom panel, we see non-Gaussian emission (with one-sided wings) from a region in the outer part of the disk. As shown in Section 4.2, we find many of these non-Gaussian emission lines in the galaxy. In some (more extreme) cases, two separate peaks can be distinguished (see bottom panels of Figure 6). As will be established and discussed in the following sections, the shapes of the lines in these cases are indicative of gas trailing behind the disk of the galaxy, or even multiple physical blobs present in the same line of sight.

4.2. Double-Component Fits

Owing to the variety and complexity of the observed emission-line profiles, in this section, we present the two-component fits to the Hα emission across the galaxy. In the following sections, we will combine the two-component fits with single-component fits to construct maps of the emission in JO201.

We refitted all of the emission lines using KUBEVIZ, setting two Gaussian components to prioritize convergence on narrow and broad components of the emission, based on the value of their velocity dispersion. The resulting fits yielded line centers ($\lambda_{\rm narrow}$ and $\lambda_{\rm broad}$), fluxes ($F_{\rm narrow}$ and $F_{\rm broad}$), and velocity dispersions ($\sigma_{\rm narrow}$ and $\sigma_{\rm broad}$) for each spaxel. From these parameters, we could then investigate in each case which component was the brightest or bluest and reveal which regions exhibited strong wings in the emission lines or double peaking. As before, we rejected fits with S/N < 3 (in either component), as well as those rejected by KUBEVIZ.

For each fitted emission line, flags were allocated based on the following parameters:

(a) 0 for spectra in which the narrow component is redward of the broad component: $\lambda_{\rm narrow} > \lambda_{\rm broad}$.

(b) $+1$ for spectra in which the narrow component is blueward of the broad component: $\lambda_{\rm narrow} < \lambda_{\rm broad}$.

(c) $+2$ where the narrow component is brighter than the broad component: $F_{\rm narrow} > F_{\rm broad}$.

(d) $+4$ where the separation between the two lines is greater than the sum in quadrature of their σ, suggesting that two distinct lines are present: $\lambda_{\rm narrow} - \lambda_{\rm broad} > (\sigma^2_{\rm narrow} + \sigma^2_{\rm broad})^{1/2}$.

For example, a region flagged as 5 will be comprised of flags $+1$ and $+4$; i.e., the narrow component will be blueward of and fainter than the broad component, with both components being significantly separated from each other.

Our flagging system allows the separation of different line profiles, as shown in Figure 6, where all of the double-component line fits are split into the different flags. For this plot, the fits were normalized to a standard velocity, width, and height to facilitate their comparison.

It is interesting to map the locations of the different line profiles in the galaxy. This is shown by the colored regions in Figure 7.

Emission lines with Flag < 3 are predominant in the center of the galaxy. These fits correspond to cases in which the two components are aligned or not significantly misaligned (see top row in Figure 6). The cause of these types of line profiles is the presence of an AGN. The active nucleus not only causes line broadening (Flag $= 0$), but, in some cases, it can generate outflows visible as mildly visible wings to one side of the broadened lines (e.g., Flag $= 1$). Lines with Flags $= 0$, 1, and 2 account for 18% of the two-component fits with S/N > 3.

Lines with Flag $= 3$ show skewed emission lines, exhibiting wings on the redward sides of bright emission lines. These trailing wing profiles are common (45%) and are typically found in the disk.

Fits with Flag $\geqslant 4$ are more extreme cases in which there is a significantly displaced second component (37% of all two-component fits; see bottom row of Figure 6). These types of fits

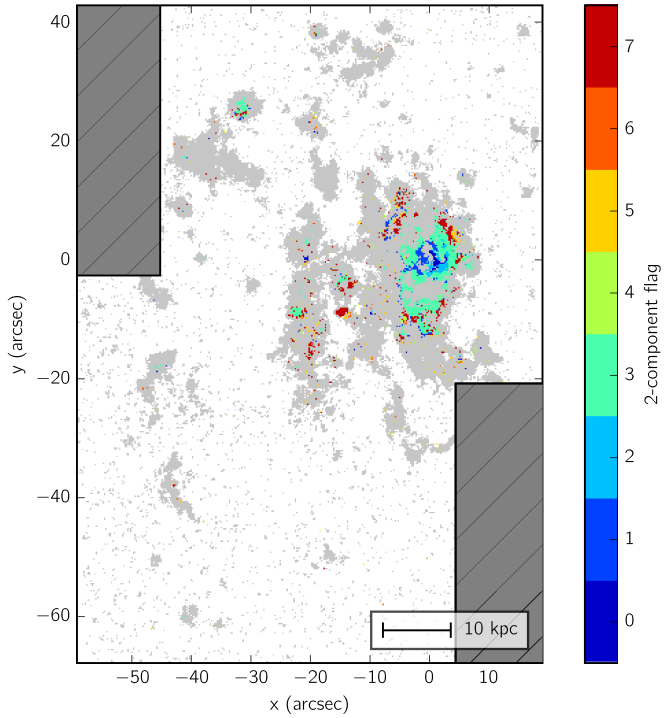

Figure 7. Map of fitted spaxels in JO201, separated into regions where double-component fits were used (colored areas) or single-component fits were sufficient to fit the Hα emission (gray areas). We chose the double-component fits when both the narrow and broad components were detected to greater than 3σ, otherwise a single component (also limited to 3σ) was used. Colors other than gray correspond to the flags attributed to each two-component fit (cf. Figure 6), as indicated by the color bar.

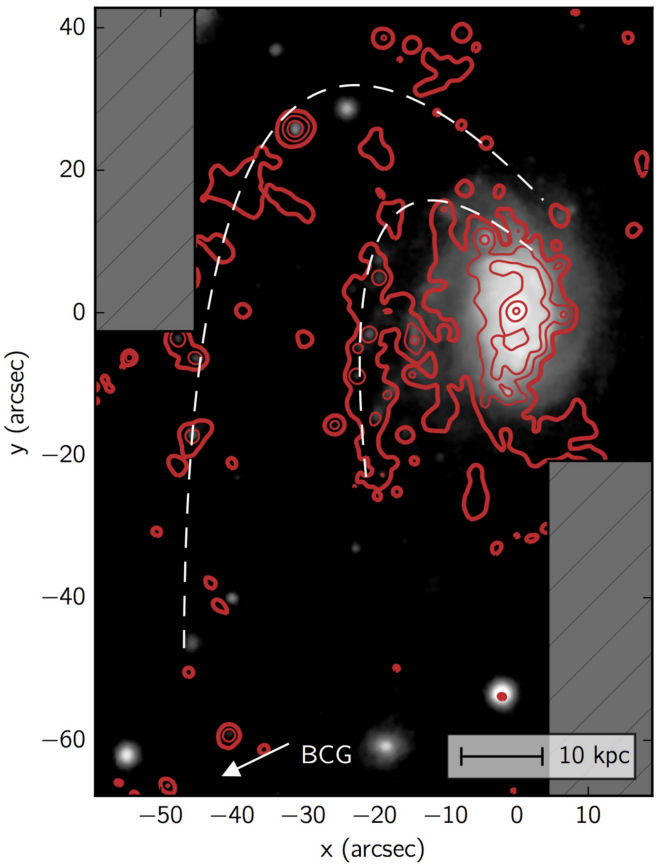

Figure 8. Contours of Hα (λ6562.82) overlaid on the continuum fit around the Hα line. Steeper contours on the western edge of the disk suggest increased star formation activity resulting from the interaction with the ICM. Contours correspond to surface brightness levels of 6.67×10^{-19}, 3.55×10^{-18}, 1.89×10^{-17}, 1.00×10^{-16}, and 5.33×10^{-16} erg s^{-1}cm^{-2} from low to high. The pattern of the stripped material appears to follow the shape of the spiral arms (white dashed curves), as discussed in the text. The white arrow indicates the direction toward the BCG.

are the best description of the emission lines in the regions around the edges of the galactic disk, as well as the diffuse regions around the stripped tails. Their location and morphology are consistent with the scenario in which JO201 is primarily undergoing gas stripping along the line of sight, with the stripped gas being dragged behind the galaxy by ram pressure. The stripped material could be arranged in the form of either a physical tail behind the galaxy or separate blobs along the same line of sight. This interpretation is in agreement with the environmental analysis presented in Section 2 and further supported by the kinematic analysis of the stellar and gaseous components of the galaxy presented in Section 5.

4.3. Final Fits

To identify the best fit in each fitted spaxel, we compare the results of the single- versus double-component fits in each case. We use the S/N of the single-component fit and the narrow and broad components of the double-component fits for this purpose.

We use the double-component fits when both the narrow and broad component are detected to greater than 3σ, otherwise a single component (also limited to 3σ) is used. Figure 7 shows the regions where double-component (colored areas) versus single-component (gray areas) fits are used. The figure shows that, although single-component fits characterize the emission in most parts of the galaxy well, two-component fits are needed in the central region and in some parts of the disk and stripped tails.

Unless otherwise stated, the abovementioned combination of single- and double-component fits is used in the rest of this analysis.

4.4. Hα Distribution

The spatial distribution of the fitted line flux in Hα is shown by red contours overlaid on the continuum fit from KUBEVIZ in Figure 8. It is visible in the figure that the emission from the Hα component shows a large offset, down to a surface brightness of $\sim 0.7 \times 10^{-18}$ erg s^{-1} cm^{-2}, from the disk of the galaxy due to the effect of RPS. Furthermore, the bright ridge of Hα on the western side of the galaxy may evidence the interaction with the hot ICM compressing the gas and forming a bowshock, increasing the star formation activity and thus the Hα emission. To the east of the galaxy disk (roughly in the direction toward the BCG, as shown by the arrow in the figure), the Hα emission is drawn out into "tentacles" of trailing gas that connect brighter knots. These knots are likely to be previously stripped gas that has collapsed under gravity to undergo intense star formation. The pattern of the diffuse emission and the collection of brighter knots observed in the plot suggest an unwinding of the spiral arm structure (white dashed curves). A possible explanation is that strong

ram-pressure "wind" can cause the spiral arms to unwind. This effect has not been observed in hydrodynamical simulations (yet) due to the difficulty of reproducing realistic spiral arms. Observationally, the effect has not been reported either, although studies of jellyfish galaxies have mostly focused on the stripping of galaxies in the plane of the sky, where the tails are more easily detected. The proposed effect, if true, would be better appreciated in galaxies like JO201 that are experiencing intense face-on stripping and are viewed along the direction of the stripping (i.e., along the line of sight). We plan to utilize simulations to address this idea in future studies.

Although the jellyfish tails in JO201 extend ∼50 kpc from the disk, it is likely that they are much larger given the strong projection effects expected for this galaxy and the fact that the stripped material covers essentially the entire field of view of the MUSE mosaic.

Our measurements are consistent with recent observations of other jellyfish galaxies in clusters. For example, from deep Hα+[N II] wide-field imaging with MegaCam at the Canada-France-Hawaii Telescope (CFHT) Boselli et al. (2016) found tails of diffuse ionized gas in NGC 4590 extending ∼80 kpc from the disk in projection (at a surface brightness limit of a few 10^{-18} erg s^{-1} cm^{-2}). Using MUSE at the VLT, Fumagalli et al. (2014) observed the jellyfish galaxy ESO 137-001 in the Norma cluster and found that, at a surface brightness of $\sim 10^{-18}$ erg s^{-1} cm^{-2}, the tails extend >30 kpc from the disk. These examples are quite different from JO201 and its environment: NGC 4590 is a very massive late-type galaxy falling into a low-mass cluster, ESO 137-001 is a lower-mass spiral falling into a very high-mass cluster, and JO201 is a massive spiral falling into a very massive cluster. Although the exact comparison of the tail extent is subject to projection effects and the depth of the observations, we can confidently conclude that the observed tails in all cases clearly extend well beyond the galaxy (out to at least 30–80 kpc), which implies that RPS has a wide range of action.

4.5. 3D Rendering of Hα Emission

To visualize the distribution of the Hα gas, a 3D model was produced by combining projected and velocity space.

The fitted Hα line was used to produce a "cleaned" cube comprised of only Hα emission. Contours were wrapped onto this surface using the velocity distribution in place of the spatial distribution of the gas along the line of sight. We selected contour levels manually to optimally separate different points of interest, such as the bright central Hα emission, the knots within the tails, and the diffuse extended gas. The resulting 3D model is presented in Figure 9. An interactive version of the figure is available in the online version of this paper and at web.oapd.inaf.it/gasp/publications.html.

Viewed face-on, the 3D model visualizes the distribution of the Hα gas and highlights the bright knots within the tails (as in Figure 8). If the cube is rotated to get a view through the *y*-axis, the rotation of the gas is visible both within the disk and in the tails, along with a dispersion-dominated nucleus. From this perspective (and also when viewing through the *x*-axis), the diffuse component of the gas can be seen at higher line-of-sight velocities than the denser knots.

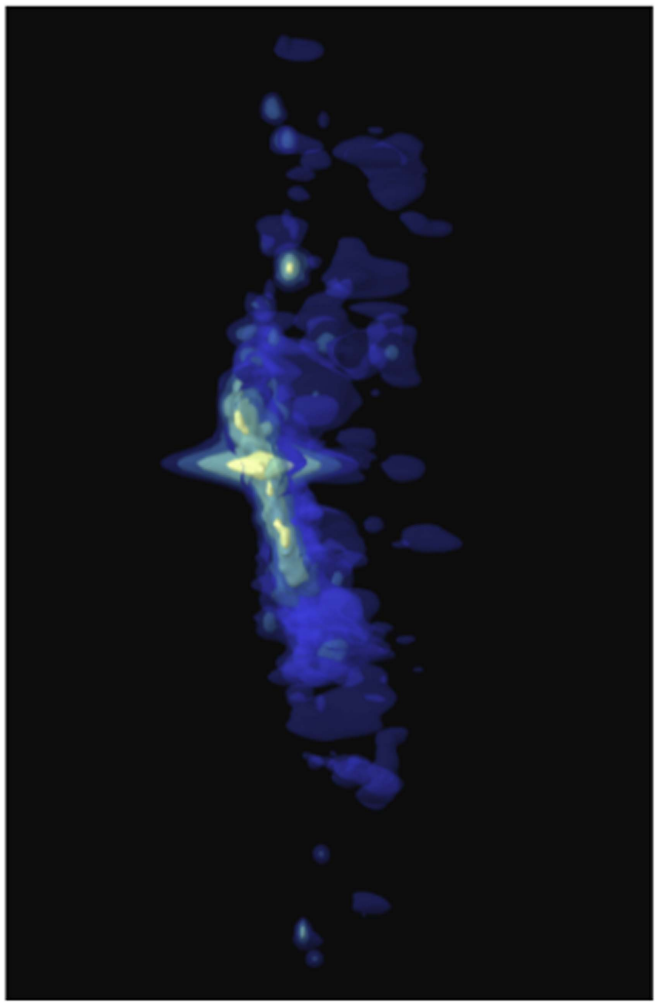

Figure 9. 3D visualization of Hα gas extracted from the KUBEVIZ fit, produced using the method presented in Vogt et al. (2016a, 2016b). The *X*- and *Y*-axes show projected distance, with the *Z*-axis representing the wavelength/velocity and line width/σ. Surface contours are plotted with different colors, from yellow to dark blue. The units and contours are arbitrary, as they have been chosen at levels that highlight interesting features in the Hα gas, such as the bright central emission, knots of Hα, and extended diffuse gas. An interactive version of this figure is accessible online in the HTML version of this paper and at web.oapd.inaf.it/gasp/publications.html.

5. Kinematics

5.1. Absorption-Line Kinematics

In order to extract the stellar kinematics, we extracted the absorption-line properties from the galactic extinction–corrected cube using the penalized pixel-fitting (pPXF) code (Cappellari & Emsellem 2004) that fits the observed spectra with a set of templates. We spatially binned the spectra using a Voronoi tessellation dependent on the S/N of our spectra (S/N = 15), as described in Cappellari & Copin (2003). In particular, we used a weighted Voronoi tessellation (Diehl & Statler 2006) in order to take care of a possible significant gradient in the S/N. For our analysis, we used the stellar population templates by Vazdekis et al. (2010), i.e., a set of single stellar population (SSP) spectra spanning a range in metallicity (six different metallicities from [M/H] = −1.71 to [M/H] = 0.22) and age (26 ages from 1 to 17.78 Gyr) calculated with a Salpeter IMF (Salpeter 1955) with a slope

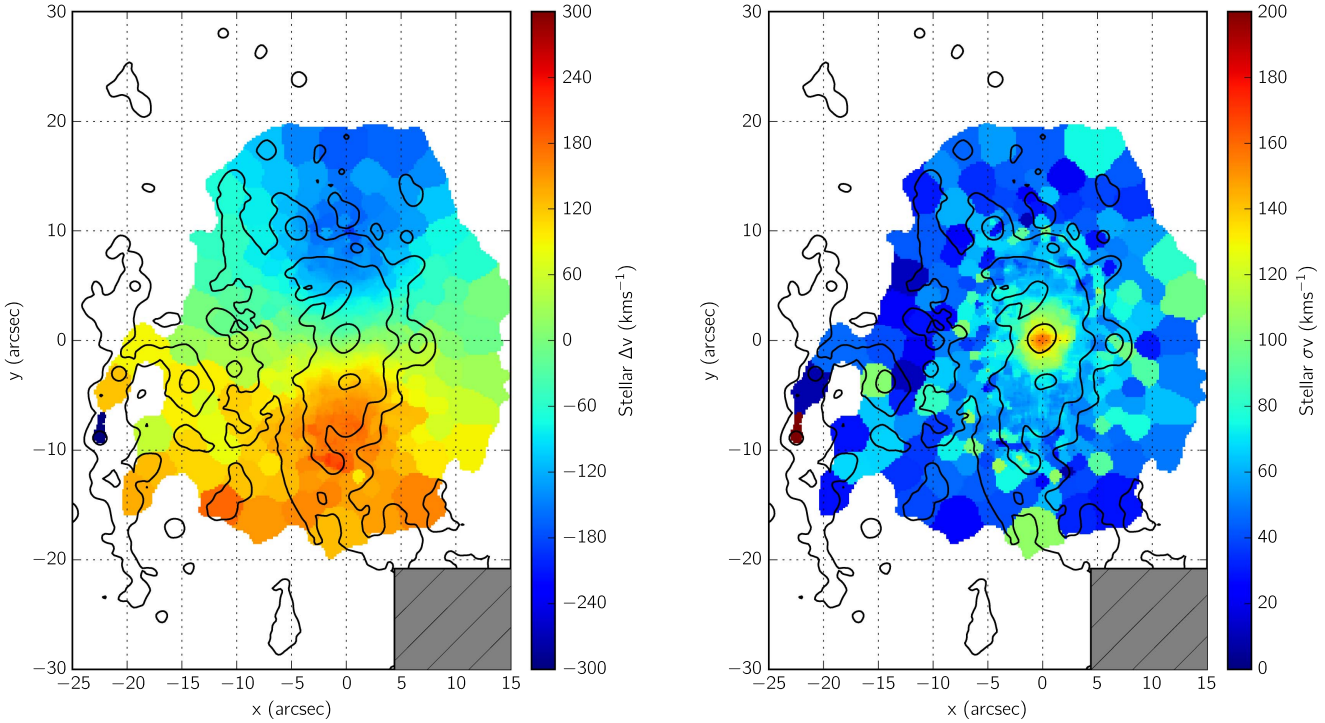

Figure 10. Stellar kinematics (left: line-of-sight velocity; right: velocity dispersion) derived from pPXF fits binned using a Voronoi tessellation to obtain an S/N of 15. The Hα contours are shown overlaid. As expected for the case of RPS, the stellar component shows smooth, generally unperturbed kinematics. This is consistent with a hydrodynamical interaction, as opposed to a gravitational one.

of 1.30 and the Padova 1994 isochrones (Bertelli et al. 1994; Girardi et al. 1996). We excluded from the fit the red part of the spectra, where the theoretical stellar libraries have poor resolution and the observed spectra are strongly contaminated by the sky lines. Spurious sources (foreground stars, background galaxies) were masked before performing the fit. We derived the rotational velocity, velocity dispersion, and two h3 and h4 moments. This allowed us to derive a redshift estimate for each Voronoi bin that will then be used as input for the stellar population analysis.

The stellar kinematics maps (not corrected for the inclination of the galaxy) are shown in Figure 10, with the velocity in the left panel and the velocity dispersion in the right panel. The velocity map shows that the stellar component follows a uniform rotation, with maximum velocity $\simeq$155 km s^{-1}. The velocity dispersion profile of this galaxy is also smooth, with increasing values toward the center that peak at $\simeq$150 km s^{-1}.

To the southeast of the disk, two parallel tails are visible. It is unlikely that these tails arise from tidal interactions, since (i) they are seen only on one side of the galaxy, (ii) spectrophotometric modeling shows that they have very young stellar populations (C. Bellhouse et al. 2017, in preparation), and (iii) they follow the main rotation of the galaxy. As will be discussed in C. Bellhouse et al. (2017, in preparation), these young stellar tails most likely formed in situ from stripped gas.

Overall, the stellar kinematics of JO201 is consistent with that of a gravitationally undisturbed galaxy.

5.2. Emission-Line Kinematics

In order to produce maps of the kinematics of the gaseous component in JO201, we extracted the velocity and velocity dispersion of the Hα (λ6562.82) line from the line fits presented in Section 4.

The left panel of Figure 11 shows a map of the line-of-sight velocities of the Hα emission (not corrected for inclination). A zoomed version focusing only on the disk (with a smaller range of velocities) is shown in the right panel of the figure. Overall, the gas component displays a clear rotation within the disk. The rotational velocity gradient of the galaxy is somewhat retained in the stripped material to at least 50 kpc in projected distance from the disk, although, beyond the central disk, the stripped material outside the galaxy's main body is notably residing at higher line-of-sight velocities (up to $\sim$900 km s^{-1}) with respect to the disk. This highly redshifted emission reflects the intense RPS acting on the galaxy along the line of sight. As the galaxy plunges toward the observer, the gas stripped from the (less-shielded) outskirts of the galaxy is dragged away from it. As already mentioned, this interpretation is in agreement with the extreme line-of-sight velocity of JO201 with respect to the cluster (Section 2), which suggests that the velocity vector of the galaxy is mostly in the line of sight; thus, the majority of the stripped material must reside behind the galaxy.

Inside the disk, the maximum observed rotational velocity of the ionized gas toward the observer is $\sim$144 km s^{-1}. It extends beyond $\sim$179 km s^{-1} away from the observer at the southern end of the disk, up to where gas starts to be visibly stripped both along the plane of the sky and in the redshift direction. From a quick comparison of the rotation of the gas (Figure 11, right) and the stars (Figure 10, left), it is noticeable that the rotational velocity of the gas is significantly higher than that of the stars. A careful comparison of the stellar and gas rotation curves is presented in Section 5.3.

We further compare the kinematics of the broad and narrow components of the Hα line in Figure 12 for those regions where a double-component fit is available. The colors in the figure highlight the difference between the velocities of the two components. The central region, showing a blueward broad

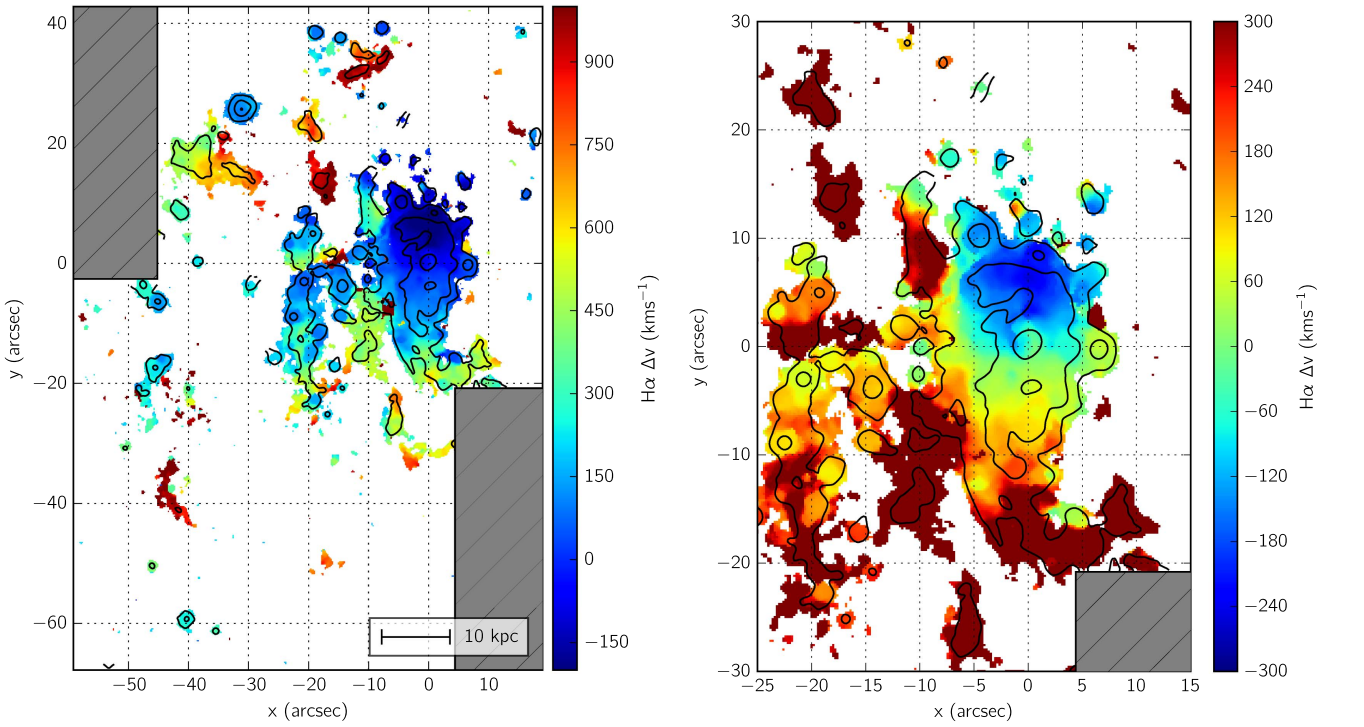

Figure 11. Left: velocity map of Hα (λ6562.82) emission relative to the galaxy systemic velocity comprised of a combination of single-component and two-component fits, as described in Section 4.2. The velocity map has been convolved with a median filter with a 3 × 3 pixel kernel for visualization purposes, in addition to the data being smoothed using a mean filter with a 3 × 3 kernel before fitting. Right: velocity map as on left, cropped to show the disk region with a rescaled color map to better exhibit the Hα kinematics of the disk region. Black contours in both panels indicate the Hα flux for context.

component, indicates a tail oriented toward the observer. This is likely to originate from an outflow associated with the central AGN. The redward broad component in the outskirts of the disk is suggestive of tails produced by increased stripping intensity at the outer edges of the disk, consistent with outside-in stripping.

The line-of-sight velocity dispersion of the gas component is shown in Figure 13. The figure shows that the velocity dispersion in the central region of the disk is 150–180 km s^{-1}. The lowest velocity dispersions are observed in the dense knots with large Hα fluxes, with typical values ranging around 20–40 km s^{-1}. The stripped diffuse gas bridging the star-forming knots appears to have a higher velocity dispersion, with values around 140 km s^{-1}.

Finally, the line-of-sight velocities of all fitted spaxels are plotted against their velocity dispersions in Figure 14. The x-axis tries to separate the disk of the galaxy from the stripped high-velocity tails, while the y-axis can be used to distinguish between collapsing and heated/shocked gas. The plot shows a bimodal distribution of line-of-sight velocities within the disk of the galaxy, visible in the lower left region of the plot ($\Delta v \lesssim 200$ km s^{-1} and $\sigma v \lesssim 70$ km s^{-1}), with a visible skew to positive velocities due to the influence of strong line-of-sight gas stripping. At velocities of $\lesssim$350 km s^{-1}, the stripped gas follows a steep increase in velocity dispersion with increasing velocity, owing to the onset of turbulent motion within the stripped gas as it moves away from the galaxy. Above 350 km s^{-1}, the trend reverses as the dispersion falls, likely due to the recollapse of cooling stripped gas.

Although the unique direction of the stripping and viewing angle of JO201 makes the comparison with other jellyfish galaxies difficult, our results are consistent with observations of

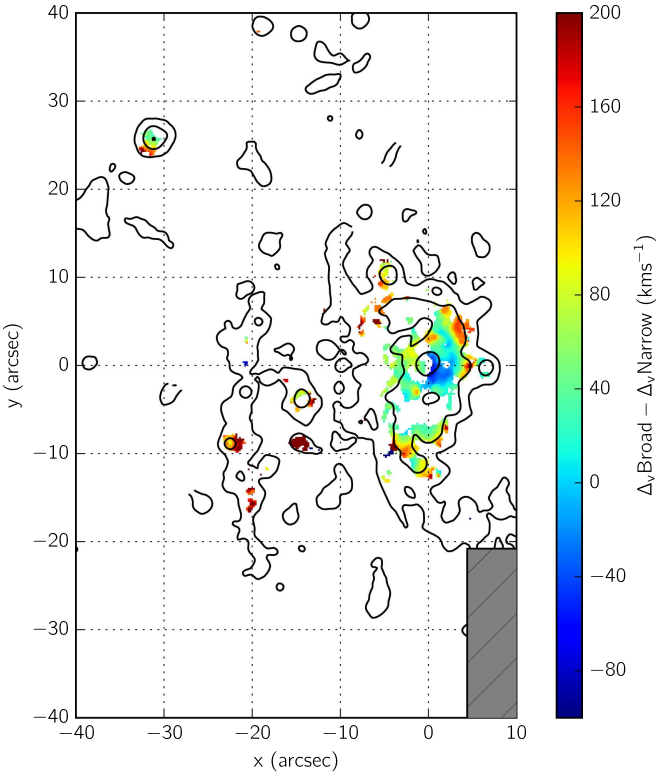

Figure 12. Velocity offset between the broad and narrow components of the Hα (λ6562.82) line where a double-component fit is available. The region of the blueward broad component, indicating a tail oriented toward the observer, is likely to originate from an outflow associated with the central AGN. The redward broad component in the outskirts of the disk evidences tails in the velocity distribution produced by increased stripping intensity at the outer edges of the disk. Black contours indicate the Hα flux for context.

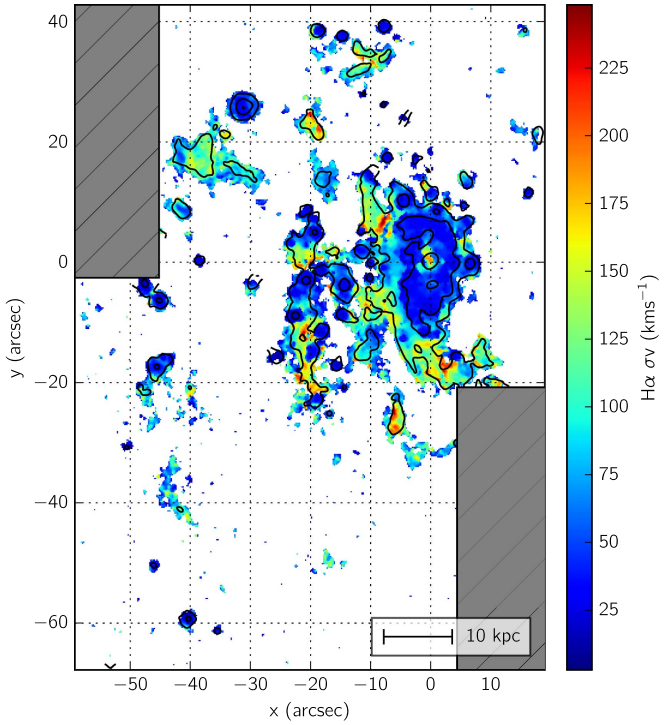

Figure 13. Velocity dispersion map produced using Hα (λ6562.82) emission from combined single-component and two-component fits as described in Section 4.2, corrected for instrument resolution by KUBEVIZ. The velocity dispersion map has been convolved with a median filter with a 3 × 3 pixel kernel for visualization purposes.

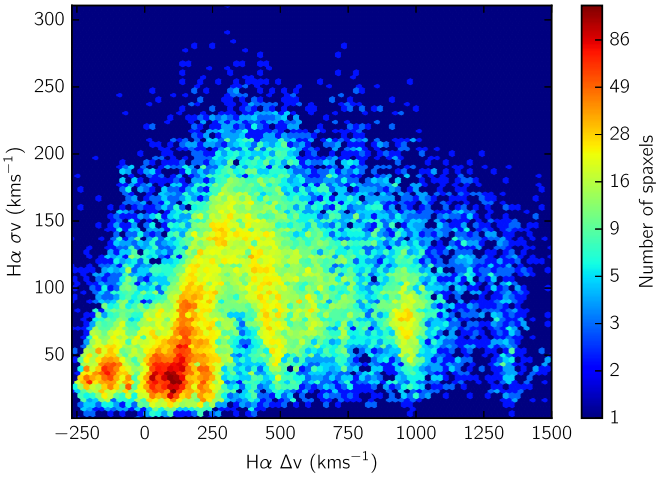

Figure 14. Distribution of spaxels arranged by velocity on the x-axis and σ on the y-axis. The plot shows a bimodal distribution around 0 km s^{-1} from the rotation curve of the galaxy, followed by an increase in dispersion with velocity due to the onset of turbulent motions within the stripped gas. This trend reverses above 350 km s^{-1} as the dispersion falls, likely caused by the recollapse of cooling stripped gas.

nearby jellyfish that show a structured distribution of the stripped gas composed of compact blobs and diffuse filaments (e.g., Boselli et al. 2016), as well as simulated RPS events (Tonnesen & Bryan 2010). Moreover, previous studies of the dynamics of jellyfish galaxies have shown that the stripped gas (primarily in the plane of the sky) preserves the rotation of the galaxy for a while (e.g., up to ∼20 kpc in ESO 137-001; Fumagalli et al. 2014), and then turbulent motion takes over. In JO201, we observe a similar phenomenon, but primarily along the line of sight.

5.3. Rotation Curves

To directly compare the distribution of the stellar component and the Hα gas in velocity space across the galaxy, we construct rotation curves.

The red curve in Figure 15 shows the rotation curve of the stellar component, constructed by taking the median velocities in a strip approximately 10″ wide along the disk's kinematic major axis (2°.5 from north to east). The Hα emission-line velocity map is plotted on top, in strips parallel to the direction of the stellar kinematic major axis, to show the overall velocity structure of the gas (black lines), as well as the spread within individual regions undergoing stripping. Velocities were corrected for galaxy inclination ($i = 54°$ from face-on) by dividing the observed velocities by $\sin i$.

The offset between the stellar and gaseous components of the disk is clearly visible in Figure 15. A large fraction of the ionized gas is redshifted with respect to the stellar disk as a consequence of strong ram-pressure drag. Interestingly, many of the individually stripped clumps of material (groups of black lines separated from the main body of the galaxy) seem to preserve the overall gradient of the rotation curve of the galaxy, although redshifted.

To test whether the high-velocity stripped gas is bound to the galaxy, we computed an upper limit to the escape velocity, $v_{\rm esc}$, using the potential of a thin exponential disk with the form presented in Equation (2.165) of Binney & Tremaine (2008),

$$\Phi(r, 0) = -\pi G \Sigma_0 r [I_0(y)K_1(y) - I_1(y)K_0(y)], \qquad (6)$$

where $y = r/2r_d$; I_n, K_n are modified Bessel functions; r_d is the disk scale length; and Σ_0 is the central surface density of a thin exponential disk calculated from the dynamical mass as $\Sigma_0 = M_{\rm dyn}/2\pi r_d^2$. To determine $M_{\rm dyn}$, we followed Equation (15) of van den Bosch (2002), using the maximum velocity values of the stellar rotation curve (∼190 km s^{-1} after correcting for an inclination of 54°, calculated from an axis ratio of ∼0.6) and an I-band disk scale length (we used 5.56 kpc, as in Section 2, because this value is consistent with fits made to the stellar continuum using the MUSE data cube). The resulting dynamical mass was found to be $M_{\rm dyn} = 5.10 \times 10^{11} M_\odot$. The calculated escape velocity ($v_{\rm esc}^2(r) = -2\Phi(r)$) is an upper limit, as it does not take into account the vertical extent of the disk. Moreover, we note that $v_{\rm esc}(r)$ should ideally be compared with the magnitude of the full velocity vector of the gas, while our observations are limited to the line-of-sight velocity component. We plot $v_{\rm esc}(r)$ as a dotted-dashed orange curve on top of the stellar rotation curve of the galaxy in Figure 15. Because it only makes sense to compare absolute values of Δv with $v_{\rm esc}$, for $r_{\rm maj} > 0$ (where the stellar rotation curve has $\Delta v < 0$), we have plotted $v_{\rm esc} + 2\Delta v$ instead.[12] The plotted line helps distinguish several clumps of stripped gas that are unbound from the disk. These are located in the outer parts of the disk lying above the line.

Figure 16 presents inclination-corrected rotation curves of the stars and the ionized gas, separated into narrow and broad

[12] This accounts for the difference in using Δv rather than $|\Delta v|$. The plotted function, $p(r)$, should obey the relation $v_{\rm esc} - |\Delta v| = p(r) - \Delta v$.

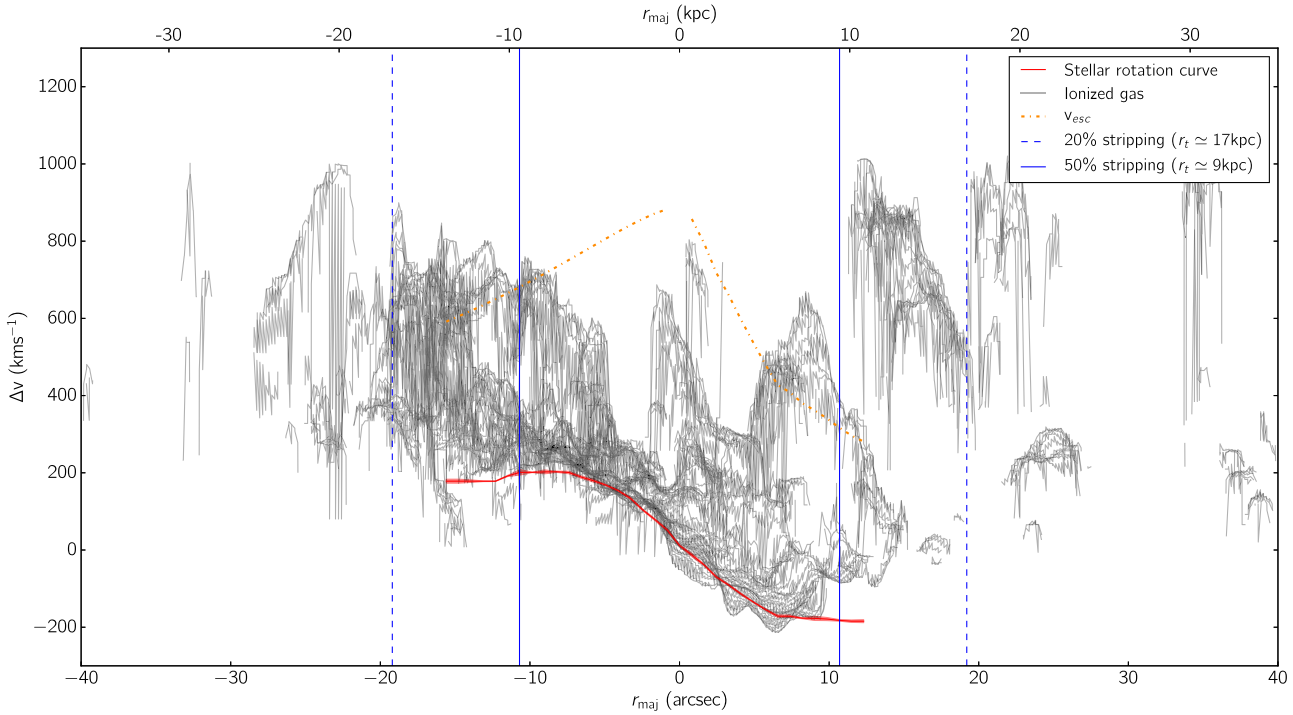

Figure 15. Rotation curve along the kinematic major axis r_{maj} for the stellar component of JO201 is plotted in red. The solid black lines show the velocity of the ionized gas along strips parallel to the direction of r_{maj}. The orange dot-dashed line shows the escape velocity calculated as described in the text. The vertical blue dashed and solid lines further show the truncation radii at which 20% and 50% of the total gas mass is expected to have been stripped, respectively, as described in Section 2 (see lines in Figure 2). The gas stripping is made clear by the increased line-of-sight velocity of the ionized gas to the left and right of the disk caused by regions of stripped gas being slowed by the ICM with respect to the infalling galaxy. Rotating clumps of gas can also be seen at higher Δv in the stripped gas, rotating around their own centers away from the motion of the galaxy. It is likely that much of this gas has become unbound from the galaxy due to its high-velocity offset, particularly where it approaches and passes the indicated escape velocity. However, the gas retains the angular momentum of its previous rotation within the galaxy. The region of gas that remains mostly bound to the disk is best illustrated by the dashed lines in Figure 16, within a diameter of ∼10 kpc (see the text for details). Measured velocities have been corrected for inclination to show the intrinsic rotational velocity.

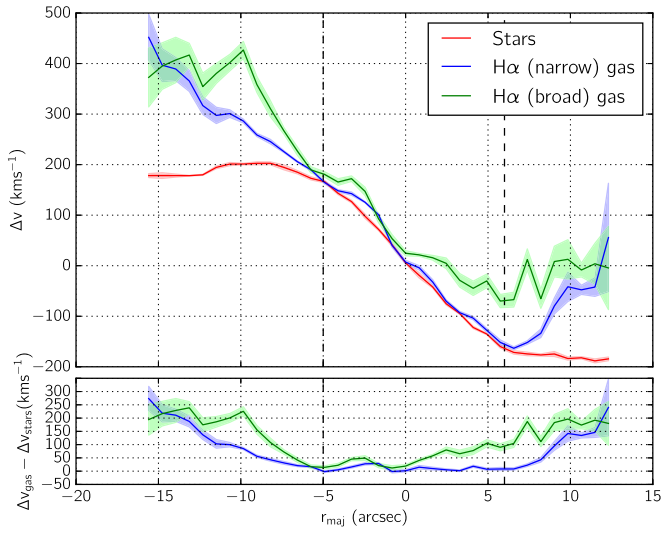

Figure 16. Rotation curves of JO201, measured within an ∼10" wide strip along the kinematic major axis r_{maj} of the stellar disk. Inclination-corrected median stellar velocities (obtained from the absorption-line kinematics) are shown in red, along with the median velocity of the ionized gas separated into the narrow (blue) and broad (green) components of the Hα emission-line fits. Standard deviations of bootstrap medians are shown for both. Dashed lines enclose the region of the disk less affected by RPS ($r_{maj} \lesssim 6$ kpc).

components of the Hα emission. All of the curves were constructed by taking the median velocities in a strip approximately 10″ wide along the disk's kinematic major axis. In the lower part of the figure, the residuals of the narrow and broad gaseous components from the stellar component are shown.

The rotation curves highlight the existing offset between the stellar and gaseous components of the disk. In particular, the rotation curve of the gaseous component shows an upward turn at the edges of the stellar disk, $|r_{maj}| \gtrsim 6''$. The residuals clearly show the increase in the velocity offset with distance from the center of the disk, with the broad component showing a more pronounced effect. Note that the difference between the blue and green lines in Figure 16 reflects the velocity offset displayed in Figure 12. The observed behavior can be interpreted as a decrease in the gravitational binding of the gas at higher distances from the center of the galaxy (see Section 2) that allows the gas to be more easily stripped from the edges of the disk.

In summary, Figures 15 and 16 highlight the intensity of the stripping experienced by JO201 with a redshifted ionized gas component with respect to the stellar disk. This is consistent with ram pressure dragging the gas away from the fast-moving galaxy (and the observer). The incremental shift in velocity observed at larger distances from the center of the galaxy indicates outside-in gas removal, and the shape of the asymmetric rotation curve of the gas is consistent with simulations of face-on RPS (Kronberger et al. 2008).

6. Summary and Conclusions

This paper is the second in a series presenting the first results from the ongoing GASP survey at the VLT (Paper I) that is

obtaining deep integral-field spectroscopy for over 100 galaxies with signatures of gas stripping (so-called "jellyfish" galaxies). We focus on the distribution and kinematics of the stellar and ionized gas components of JO201, one of the most striking jellyfish galaxies in the GASP survey and its parent sample (Poggianti et al. 2016).

We started by studying the global environment of JO201 and found that it is part of a massive unrelaxed galaxy cluster (Abell 85). Its large differential line-of-sight velocity with respect to the cluster and (projected) proximity to the BCG indicate that JO201 is likely falling into the cluster for the first time, following a radial orbit mostly in the direction toward the observer. Moreover, a dynamical analysis utilizing all the cluster members suggests that JO201 is possibly falling into Abell 85 within a small group of galaxies.

JO201 has been classified as a jellyfish galaxy candidate by Poggianti et al. (2016) owing to the presence of optical tails on only one side of the galaxy, which suggests that unilateral gas stripping is taking place. We modeled the ram pressure expected in Abell 85 and found that, at the projected position and velocity of JO201, a galaxy of its mass and size must have lost $\sim$50% of its total gas mass during its first passage through the cluster. The amount of lost gas coincides remarkably well with the estimated gas loss computed by comparing the size of the stellar disk with the extent of the remaining Hα (ionized gas) disk. Our environmental analysis thus strongly supports RPS as the principal mechanism removing gas from JO201 during its first passage through the dense ICM.

We analyzed the MUSE data cubes (covering JO201's main body and outskirts) to study the distribution and kinematics of the stellar and ionized gas components of the galaxy and found the following.

1. There is significant Hα emission concentrated along the windward side of the galaxy (colliding with the ICM), as well as tails in the opposite direction composed of bright Hα knots and diffuse emission. The tails extend $\sim$50 kpc away from the galaxy and point toward the cluster center. The observed (structured) distribution of the gas is consistent with RPS simulations of galaxies (Tonnesen & Bryan 2010). We identify a pattern in the distribution of stripped gas in the tails of JO201 that resembles the shape of wide spiral arms. If true, a possible explanation is that strong RPS can cause an unwinding of the outer spiral arms. Owing to the difficulty of reproducing realistic spiral arms in simulated galaxies, this effect has not (yet) been reported by simulations of RPS. Observations of other jellyfish galaxies have not reported the effect either, but this is likely a consequence of the rare angle of observation of JO201. We hope to explore and expand upon this idea in future GASP studies.
2. In some parts of the galaxy, the Hα emission often displays a non-Gaussian profile. We characterize the different types of line profiles within the galaxy and find that, at the center of the galaxy, there is emission-line broadening caused by an active nucleus. In the outer parts of the disk and stripped tails, the emission lines can be described by either a single narrow Gaussian or a narrow component with an offset (redward) broader component. These double-Gaussian profiles result from intense gas stripping along the line of sight that drags material away from the galaxy (in the opposite direction from the observer).
3. After selecting the best fit (single- versus double-component Gaussians) in each spaxel, we construct a three-dimensional model of the Hα emission in the galaxy that highlights the extent of the emission-line wings in the redshift direction.
4. From a kinematic analysis of the absorption features, we find that the velocity field of the stellar component is well reproduced by a smoothly rotating disk. This suggests that there are no gravitational perturbations, such as tidal interactions, acting on JO201. The velocity of the gaseous component follows that of the stars in the inner regions of the galaxy but deviates significantly from the disk to the tails. In particular, much of the stripped material with Hα emission resides at a higher line-of-sight velocity with respect to the stellar disk. The trend, clearly seen in the rotation curves of the stellar and gaseous components, increases with distance from the galaxy center, in agreement with simulations of face-on RPS (Kronberger et al. 2008).
5. The velocity dispersion in the stripped diffuse gas is high ($>100\,\mathrm{km\,s^{-1}}$), while the star-forming blobs are kinematically cold (velocity dispersion $<40\,\mathrm{km\,s^{-1}}$), suggestive of shock heating and gas compression, respectively.

Overall, our results favor RPS as the main mechanism removing gas from JO201. This galaxy's trajectory in the cluster, together with our viewing angle, offers a unique insight into the ram-pressure drag generated by the ICM, with most of the stripping happening along our line of sight as the galaxy plunges through the cluster toward the observer. Moreover, the MUSE observations reveal clear evidence for outside-in RPS of the disk, with gas compression and shock heating occurring in the stripped tails. In a forthcoming paper (C. Bellhouse et al. 2017, in preparation), we will further investigate the sources of ionization in this galaxy, along with an analysis of the gas-mass loss, gas-phase metallicity, and ages of the stellar populations across the galaxy.

JO201 is an extreme case of stripping of a massive galaxy ($\sim10^{11}\,M_{\odot}$) in a massive ($\sim10^{15}\,M_{\odot}$) cluster. Our results are consistent with previous studies of jellyfish galaxies in a variety of environments and thus highlight the importance and wide range of action that RPS has on satellite galaxies.

We would like to thank the anonymous referee for helping improve the paper significantly. This work is based on observations collected at the European Organisation for Astronomical Research in the Southern Hemisphere under ESO program 196.B-0578. This work made use of the KUBEVIZ software, which is publicly available at http://www.mpe.mpg.de/~dwilman/kubeviz/. We thank Matteo Fossati and Dave Wilman for their invaluable help with KUBEVIZ. C.B. thanks Frederic Vogt for the advice on data visualization and on producing and presenting 3D visualizations of emission lines. We thank Graeme Candlish for useful discussions. This work was cofunded under the Marie Curie Actions of the European Commission (FP7-COFUND). We acknowledge financial support from PRIN-INAF 2014. JF acknowledges financial support from a UNAM-DGAPA-PAPIIT IA10+15 grant, México. B.V. acknowledges support from an Australian Research Council Discovery Early Career Researcher Award (PD0028506).

References

Abadi, M. G., Moore, B., & Bower, R. G. 1999, MNRAS, 308, 947
Bacon, R., Accardo, M., Adjali, L., et al. 2010, Proc. SPIE, 7735, 773508
Baldry, I. K., Balogh, M. L., Bower, R. G., et al. 2006, MNRAS, 373, 469
Balogh, M. L., Navarro, J. F., & Morris, S. L. 2000, ApJ, 540, 113
Bekki, K., & Couch, W. J. 2003, ApJL, 596, L13
Bertelli, G., Bressan, A., Chiosi, C., Fagotto, F., & Nasi, E. 1994, A&AS, 106
Binney, J., & Tremaine, S. 2008, Galactic Dynamics (2nd ed.; Princeton, NJ: Princeton Univ. Press)
Boselli, A., Cortese, L., Boquien, M., et al. 2014, A&A, 564, A66
Boselli, A., Cuillandre, J. C., Fossati, M., et al. 2016, A&A, 587, A68
Boselli, A., & Gavazzi, G. 2006, PASP, 118, 517
Boselli, A., Gavazzi, G., Lequeux, J., et al. 1997, A&A, 327, 522
Bravo-Alfaro, H., Caretta, C. A., Lobo, C., Durret, F., & Scott, T. 2009, A&A, 495, 379
Byrd, G., & Valtonen, M. 1990, ApJ, 350, 89
Calvi, R., Poggianti, B. M., & Vulcani, B. 2011, MNRAS, 416, 727
Cappellari, M., & Copin, Y. 2003, MNRAS, 342, 345
Cappellari, M., & Emsellem, E. 2004, PASP, 116, 138
Cardelli, J. A., Clayton, G. C., & Mathis, J. S. 1989, ApJ, 345, 245
Cava, A., Bettoni, D., Poggianti, B. M., et al. 2009, A&A, 495, 707
Cavaliere, A., & Fusco-Femiano, R. 1976, A&A, 49, 137
Cayatte, V., van Gorkom, J. H., Balkowski, C., & Kotanyi, C. 1990, AJ, 100, 604
Chabrier, G. 2003, PASP, 115, 763
Chen, Y., Reiprich, T. H., Böhringer, H., Ikebe, Y., & Zhang, Y.-Y. 2007, A&A, 466, 805
Chung, A., van Gorkom, J. H., Kenney, J. D. P., Crowl, H., & Vollmer, B. 2009, AJ, 138, 1741
Chung, A., van Gorkom, J. H., Kenney, J. D. P., & Vollmer, B. 2007, ApJL, 659, L115
Cortese, L., Davies, J. I., Pohlen, M., et al. 2010, A&A, 518, L49
Cortese, L., Marcillac, D., Richard, J., et al. 2007, MNRAS, 376, 157
Cowie, L. L., & Songaila, A. 1977, Natur, 266, 501
Diehl, S., & Statler, T. S. 2006, MNRAS, 368, 497
Dressler, A. 1980, ApJ, 236, 351
Dressler, A., & Shectman, S. A. 1988, AJ, 95, 985
Durret, F., Lima Neto, G. B., & Forman, W. 2005, A&A, 432, 809
Ebeling, H., Stephenson, L. N., & Edge, A. C. 2014, ApJL, 781, L40
Evrard, A. E. 1991, MNRAS, 248, 8P
Faltenbacher, A., & Diemand, J. 2006, MNRAS, 369, 1698
Fasano, G., Marmo, C., Varela, J., et al. 2006, A&A, 445, 805
Fossati, M., Fumagalli, M., Boselli, A., et al. 2016, MNRAS, 455, 2028
Fossati, M., Gavazzi, G., Boselli, A., & Fumagalli, M. 2012, A&A, 544, A128
Fujita, Y. 1998, ApJ, 509, 587
Fujita, Y., & Nagashima, M. 1999, ApJ, 516, 619
Fumagalli, M., Fossati, M., Hau, G. K. T., et al. 2014, MNRAS, 445, 4335
Gavazzi, G., Boselli, A., Pedotti, P., Gallazzi, A., & Carrasco, L. 2002, A&A, 396, 449
Girardi, L., Bressan, A., Chiosi, C., Bertelli, G., & Nasi, E. 1996, A&AS, 117, 113
Gullieuszik, M., Poggianti, B., Fasano, G., et al. 2015, A&A, 581, A41
Gunn, J. E., & Gott, J. R., III 1972, ApJ, 176, 1
Haines, C. P., Pereira, M. J., Smith, G. P., et al. 2015, ApJ, 806, 101
Haynes, M. P., & Giovanelli, R. 1984, AJ, 89, 758
Hester, J. A., Seibert, M., Neill, J. D., et al. 2010, ApJL, 716, L14
Ho, I.-T., Kewley, L. J., Dopita, M. A., et al. 2014, MNRAS, 444, 3894
Ichinohe, Y., Werner, N., Simionescu, A., et al. 2015, MNRAS, 448, 2971
Jaffé, Y. L., Smith, R., Candlish, G. N., et al. 2015, MNRAS, 448, 1715
Jaffé, Y. L., Verheijen, M. A. W., Haines, C. P., et al. 2016, MNRAS, 461, 1202
Kenney, J. D. P., Geha, M., Jáchym, P., et al. 2014, ApJ, 780, 119
Kenney, J. D. P., & Koopmann, R. A. 1999, AJ, 117, 181
Kenney, J. D. P., van Gorkom, J. H., & Vollmer, B. 2004, AJ, 127, 3361
Kenney, J. D. P., & Young, J. S. 1989, ApJ, 344, 171
Kronberger, T., Kapferer, W., Unterguggenberger, S., Schindler, S., & Ziegler, B. L. 2008, A&A, 483, 783
Larson, R. B., Tinsley, B. M., & Caldwell, C. N. 1980, ApJ, 237, 692
McPartland, C., Ebeling, H., Roediger, E., & Blumenthal, K. 2016, MNRAS, 455, 2994
Merluzzi, P., Busarello, G., Dopita, M. A., et al. 2013, MNRAS, 429, 1747
Merritt, D. 1983, ApJ, 264, 24
Mihos, J. C., & Hernquist, L. 1994, ApJL, 425, L13
Moore, B., Katz, N., Lake, G., Dressler, A., & Oemler, A. 1996, Natur, 379, 613
Moore, B., Lake, G., & Katz, N. 1998, ApJ, 495, 139
Moretti, A., Gullieuszik, M., Poggianti, B., et al. 2017, A&A, 599, A81
Moretti, A., Poggianti, B. M., Fasano, G., et al. 2014, A&A, 564, A138
Navarro, J. F., Frenk, C. S., & White, S. D. M. 1996, ApJ, 462, 563
Owers, M. S., Couch, W. J., Nulsen, P. E. J., & Randall, S. W. 2012, ApJL, 750, L23
Peng, Y.-j., Lilly, S. J., Kovač, K., et al. 2010, ApJ, 721, 193
Poggianti, B. M., Fasano, G., Omizzolo, A., et al. 2016, AJ, 151, 78
Poggianti, B. M., Moretti, A., Gullieuszik, M., et al. 2017, ApJ, 844, 48 (Paper I)
Quilis, V., Moore, B., & Bower, R. 2000, Sci, 288, 1617
Rawle, T. D., Altieri, B., Egami, E., et al. 2014, MNRAS, 442, 196
Roediger, E., & Brüggen, M. 2007, MNRAS, 380, 1399
Salpeter, E. E. 1955, ApJ, 121, 161
Schlafly, E. F., & Finkbeiner, D. P. 2011, ApJ, 737, 103
Smith, R. J., Lucey, J. R., Hammer, D., et al. 2010, MNRAS, 408, 1417
Spitzer, L., Jr., & Baade, W. 1951, ApJ, 113, 413
Springel, V. 2000, MNRAS, 312, 859
Takeda, H., Nulsen, P. E. J., & Fabian, A. C. 1984, MNRAS, 208, 261
Tinsley, B. M., & Larson, R. B. 1979, MNRAS, 186, 503
Tonnesen, S., & Bryan, G. L. 2009, ApJ, 694, 789
Tonnesen, S., & Bryan, G. L. 2010, ApJ, 709, 1203
Tonnesen, S., & Bryan, G. L. 2012, MNRAS, 422, 1609
Toomre, A. 1977, in Proc. Conf. at Yale Univ., Evolution of Galaxies and Stellar Populations, ed. B. M. Tinsley, R. B. G. Larson, & D. Campbell (New Haven, CT: Yale Univ. Observatory), 401
Valluri, M. 1993, ApJ, 408, 57
van den Bosch, F. C. 2002, MNRAS, 332, 456
Vazdekis, A., Sánchez-Blázquez, P., Falcón-Barroso, J., et al. 2010, MNRAS, 404, 1639
Veilleux, S., Cecil, G., & Bland-Hawthorn, J. 2005, ARA&A, 43, 769
Verdes-Montenegro, L., Yun, M. S., Williams, B. A., et al. 2001, A&A, 377, 812
Vogt, F. P. A., Owen, C. I., Verdes-Montenegro, L., & Borthakur, S. 2016a, ApJ, 818, 115
Vogt, F. P. A., Seitenzahl, I. R., Dopita, M. A., & Ruiter, A. J. 2016b, PASP, 129, 975
Vollmer, B., Cayatte, V., Balkowski, C., & Duschl, W. J. 2001, ApJ, 561, 708
Vollmer, B., Wong, O. I., Braine, J., Chung, A., & Kenney, J. D. P. 2012, A&A, 543, A33
Yagi, M., Yoshida, M., Komiyama, Y., et al. 2010, AJ, 140, 1814
Yoon, Y., Im, M., & Kim, J.-W. 2017, ApJ, 834, 73
Yoshida, M., Yagi, M., Komiyama, Y., et al. 2008, ApJ, 688, 918